Ceramics International 46 (2020) 15137–15145

Contents lists available at ScienceDirect

Ceramics International

journal homepage: www.elsevier.com/locate/ceramint

Mechanical characterisation and machining evaluation of ceramic cutting tools functionally graded with six layers

M. Bertolete[a,b,*], P.A. Barbosa[a,c], W. de Rossi[c], C. Fredericci[d], I.F. Machado[e]

[a] Universidade Federal do Espírito Santo, Departamento de Engenharia Mecânica, Vitória, 29075-910, Brazil
[b] Escola de Engenharia de São Carlos, Programa de Pós-graduação em Engenharia de Produção, São Carlos, 13566-590, Brazil
[c] Instituto de Pesquisas Energéticas e Nucleares, Centro de Lasers e Aplicações, São Paulo, 05508-000, Brazil
[d] Instituto de Pesquisas Tecnológicas, Laboratório de Metalurgia e Materiais Cerâmicos, São Paulo, 05508-901, Brazil
[e] Escola Politécnica, Universidade de São Paulo, São Paulo, 05508-010, Brazil

ARTICLE INFO

Keywords:
Functionally graded materials
Cutting tools
Sintering
Mechanical properties

ABSTRACT

Functionally graded materials (FGMs) are composites graded in one or more directions by the mean volume fraction variation of their constituents in a continuous or stepwise design. The objective of this study is to apply the FGM concept to ceramic cutting tools to widen its application range. Thus, two cutting tool materials were selected: cemented carbide, owing to its higher toughness, and alumina-based ceramic, owing to its high wear resistance at elevated temperatures. Ceramics based on alumina were functionally graded with cemented carbide and sintered using the spark plasma sintering technique. The thermal residual stresses were predicted; additionally, the microstructure, relative density, and Vickers hardness and fracture toughness for the alumina layer were evaluated, and flexural strength and machining tests were conducted. From the results, cracks were not observed in the microstructure and full density was obtained. In general, the hardness and fracture toughness values were close to those in the literature. A flexural strength improvement of at least 50% on FGM samples was observed in comparison to homogeneous ceramic ones. The FGM cutting tools supported approximately 1000 N of machining force without catastrophic failure when turning martensitic stainless steel into a conventional lathe. The values of surface roughness (Ra and Rz) agree with those in the literature under similar cutting and geometry conditions.

1. Introduction

Functionally graded materials (FGMs) can be considered as composites made of materials with distinct properties [1]. Miyamoto et al. [2] defined the basic structural unit of an FGM as an element, in which the composition and structure gradually change throughout its volume. According to Mott and Evans [3], the gradient may have a continuous or stepwise structure. Watanabe and Sato [4] and Udupa et al. [5] stated that for the former, the composition varies continuously, whereas for the latter, the change occurs in a multilayer feature. Naebe and Shirvanimoghaddam [6] said that the gradient leads to a gradual change in properties, including mechanical, physical, chemical, and electrical properties. Kawasaki and Watanabe [7] stated that homogenous materials cannot tailor properties to achieve a customised function; hence, FGMs can be classified as a distinct category of composite materials. FGM has drawn attention as a solution for some problems. Naebe and Shirvanimoghaddam [6] noted its applicability in aerospace, biomedical, and nuclear areas, whereas Kawasaki and Watanabe [7] included electrical, chemical, and optical fields. Murshed et al. [8] utilised piezoelectric actuators, and Ma and Tan [9] included ballistic applications. All of them mentioned the applicability of FGM for structural improvements.

The synthesis of FGM can be classified into three processes based on the use of gas, liquids, or solids. A successful approach for FGM development to achieve the design objectives should account for the Thoma's interactive tetrahedron, which considers the mechanical behaviour of materials, as pointed out by Meyers and Chawla [10] and Kawasaki and Watanabe [7]. The FGM performance can be hugely influenced if the complex relationships in the field of mechanical properties, characterisation, theory and processing was understood. According to Ma and Tan [9] and Udupa et al. [5], the powder metallurgy process is the most common approach for fabricating FGM, because it allows a wide range of materials to mix, microstructure control from sintering operation parameters, and shape control.

* Corresponding author. Universidade Federal do Espírito Santo, Departamento de Engenharia Mecânica, Vitória, 29075-910, Brazil.
E-mail address: marcelo.b.carneiro@ufes.br (M. Bertolete).

https://doi.org/10.1016/j.ceramint.2020.03.048
Received 5 September 2019; Received in revised form 1 March 2020; Accepted 4 March 2020
Available online 05 March 2020
0272-8842/

Table 1
Characteristics and properties of the powders used.

Powders	Particle Size [μm]	Density [g/cm^3]	Elastic modulus [GPa]	Thermal expansion coefficient [x10^{-6}°C^{-1}]
Al_2O_3–ZrO_2	0.2	4.55	351	9.11
Al_2O_3–TiC	0.2	4.26	420	8.24
WC-Co	1.5	14.90	664	5.57

Miyamoto et al. [2] stated that spark plasma sintering (SPS) is one of most advanced sintering methods. Gillia and Caillens [11] highlighted SPS as a suitable technique for FGM sintering. According to Tokita [12], the SPS system has a power generator that applies an On-Off DC pulse with low-voltage (tens of volts) and high-current (thousands of amperes) on the die and consequently on the powder to encourage sintering. In addition, the machine can simultaneously apply a uniaxial mechanical load through electrode-punches. The powders are placed in a die, typically made of graphite, and they are heat treated by electric current due to the Joule effect and/or heat transfer, depending on the material. The SPS process occurs in a controlled atmosphere of vacuum, air, or inert gas. The thermal cycle, loading cycle, displacement, and environmental control are created electronically. Orrù et al. [13] pointed out that this technique has technological and economic advantages over conventional ones, such as faster heating rate, lower sintering temperature, shorter dwell time, and lack of need for cold compaction, which makes it more efficient and usually induces microstructural improvements, energy savings, and productivity increases.

Ceramics based on alumina are interesting cutting tool materials. Trent and Wright [14] highlight their greater hardness retention, compressive strength, and chemical inertness at elevated temperatures over those of tungsten-cemented carbides. However, ceramics based on alumina have lower toughness, transverse rupture strength of approximately one-third of that of cemented carbides, high thermal expansion coefficient, and low thermal conductivity; as pointed out by Zhao et al. [15], these make the ceramics sensitive to mechanical and thermal shocks. As stated by Gong et al. [16], these disadvantages severely limit the applicability of alumina-based cutting tools. Thus, Gillia and Caillens [11] expressed the desirability of a single element that can change from hard behaviour (wear resistant) on the surface to more ductile behaviour (toughness) in the bulk.

FGM studies for cutting tools have been conducted for some tool materials groups. In Lengauer and Dreyer [17], WC-Ti(C,N)–Co-based cemented carbide was sintered in a nitrogen-free atmosphere to develop FGM cutting tools near the surface. Hence, an outward diffusion of nitrogen from the compact generates a depletion of fcc carbonitrides, such as Ti(C,N) and (Ti,W) (C,N), as well as an enriched zone of binder at the surface. Consequently, it has a zone with increased toughness that can prevent crack propagation from CVD coatings. Conversely, a Ti inward diffusion exists, inducing a transition of carbonitrides towards the bulk with an increase in hardness, but without a large mismatch of residual stress. Ji et al. [18] produced cermet cutting tools that were functionally graded by using TiB_2–TiC cermet at the surface and Ti(C,N) cermet at the substrate. Owing to the thermodynamical coupling between N and Ti, outward N diffusion occurs from the substrate to the surface, whereas Ti diffuses inward, as previously mentioned. Thus, an intermediate layer is formed. This FGM was characterised by elevated hardness at the surface with an increase in fracture toughness in the substrate direction. The authors machined 17–14 PH stainless steel and observed that the FGM cutting tool had longer tool life and better surface roughness. For ceramic FGM, Xing et al. [19] modelled and fabricated an Al_2O_3 ceramic tool that was functionally graded with TiC. The authors observed an increase in fracture toughness from the surface to the bulk and, consequently, a higher fracture strength. Gong et al. [16] fabricated a graded ceramic tool in a multidimensional manner, varying the gradation orientation angle. TiC was used as a matrix and Al_2O_3 as the secondary phase; they also used Ni and Mo as binder and NiO and MgO to aid the sintering. The most interesting result is the crack deflection due to the gradient and its orientation angle.

Based on the literature, it can be observed that FGM cutting tools were developed from the variation of the constituents of certain groups of cutting tool materials, i.e., by varying the elements composing the cemented carbide, cermet, or alumina. The objective of this study is to use two groups of cutting materials and apply the FGM concept to fabricate samples of ceramics based on alumina functionally graded with tungsten cemented carbide by using the SPS technique to improve mechanical properties and consequently widen the ceramic applicability. The thermal residual stresses were predicted. The microstructure, relative density, Vickers hardness, and fracture toughness for the alumina layer, as well as the flexural strength and machining tests were evaluated.

2. Methodology

2.1. Materials and design of FGMs

Aluminium oxide (α-Al_2O_3, 99.99% purity, 0.2 μm average particle size) mixed with zirconium oxide stabilised by 3 mol% yttrium oxide (ZrO_2–$3Y_2O_3$, 99.5%, 0.04 μm) and aluminium oxide mixed with titanium carbide (TiC, 98%, 0.08 μm) were used as the ceramics based on alumina powders in this study. NanoAmor supplied these powders. Moreover, cemented carbide (WC–Co, 1.5 μm) with 6 wt% of cobalt by Sandvik was used as a second cutting tool material to improve toughness. Table 1 lists the characteristics of the powders and some properties used to estimate the thermal residual stress in FGMs.

Two types of ceramic cutting tools based on FGMs were designed: (1) FGM Al_2O_3–ZrO_2 + WC-Co (or FGM AlZr) and (2) FGM Al_2O_3–TiC + WC-Co (or FGM AlTiC). The FGM's structural design was based on the thermal residual stress model described by Ravichandran [20]. This model was used to avoid thermal cracking or delamination due to heating or cooling during the sintering step. As the volume fractions of alumina and cemented carbide vary across the sample thickness (y), the mechanical and thermophysical properties also vary. Hence, the equations of elastic modulus ($E(y)$) and thermal expansion coefficient ($\alpha(y)$) are taken from Lanhe [21], knowing that the difference between the thermal expansion coefficients of the materials is lesser than 10x10^{-6}°C^{-1}. There are two main contributions to the total thermal residual stresses (σ_{res}) in the FGM sample: the stress equilibrium (σ_r), due to contraction and expansion; and moment equilibrium (M_t) due to stress distribution variation. The residual stresses, $\sigma_r(y)$, are obtained from the superposition of the tensile and compression stresses across the thickness (y direction), Eq. (1).

$$\sigma_r(y) = \underbrace{\alpha(y)E(y)\Delta T}_{\text{Tensile stresses}} - \underbrace{E(y)\frac{\int_{-y}^{y}\alpha(y)E(y)\Delta T}{\int_{-y}^{y}E(y)dy}}_{\text{Compressive stresses}} \quad (1)$$

The absence of constraints would lead the FGM sample to bend owing to the stress variation across the thickness. From the moment equilibrium given by Eq. (2), bending stresses arise, as shown in Eq. (3).

$$M_t = \int_{-y}^{y}\sigma_r(y)ydy \quad (2)$$

$$\sigma_b(y) = M_t E(y) \frac{y\int_{-y}^{y} E(y)dy - \int_{-y}^{y} E(y)ydy}{\int_{-y}^{y} E(y)dy \int_{-y}^{y} E(y)y^2dy - \left[\int_{-y}^{y} E(y)ydy\right]^2} \quad (3)$$

The total residual stresses, $\sigma_{res}(y)$, are defined as the stress equilibrium plus the bending stress due to the moment equilibrium, as shown in Eq. (4).

$$\sigma_{res}(y) = E(y)\left[\alpha(y) - \frac{A_1}{E_1} + \frac{\left\{A_2 - \frac{A_1}{E_1}E_2\right\}\{yE_1 - E_2\}}{\{E_1E_3 - E_2^2\}}\right]\Delta T \quad (4)$$

In which, $A_1 = \int_{-y}^{y} \alpha(y)E(y)dy$; $A_2 = \int_{-y}^{y} \alpha(y)E(y)ydy$; $E_1 = \int_{-y}^{y} E(y)dy$; $E_2 = \int_{-y}^{y} E(y)ydy$; $E_3 = \int_{-y}^{y} E(y)y^2dy$; and ΔT is the temperature variation in sintering. This model simplifies and assumes that the elastic moduli and thermal expansion coefficients are independent of temperature.

2.2. FGMs processing

Based on the thermomechanical model, the volume fraction of constituents for the two FGMs were defined as shown in Table 2, with six layers in the substrate.

The powders were mixed for 1 h in a liquid environment of isopropyl alcohol with cemented carbide as the milling element in a mass ratio of 1:1. Next, they were dried for 24 h in a laboratory drying oven (model 404D by Ethik) and mechanically deagglomerated for 1 h.

The loose powders were manually placed in a graphite die (grade ED-3 by Morganite) layer by layer in preparation for sintering. The powder mass for each layer was measured using a precision scale with 0.001 g resolution (model 200 CE by Marte). Previously, the internal wall of the graphite die was wrapped with a graphite sheet (Grafoil GTB by Morganite) to prevent adhesion among the powders, punches, and die wall, apart from facilitating the sintered removal; as depicted in Fig. 1.

The sintering step was performed in a Spark Plasma Sintering (SPS) machine, model SPS 1050 by SPS Syntex Inc. DC pulse pattern 12 On 2 Off with 3.3 ms/pulse was used. The sintering parameters were a uniaxial pressure of 70 MPa, a temperature of 1300 °C and a dwell time of 5 min. The heating and cooling rates were 100 and 70 °C/min, respectively. The FGM samples were sintered to have a diameter of approximately 20 mm and a thickness of 8 mm. These samples were used in density, hardness, fracture toughness and machining evaluations. Homogeneous ceramics were also sintered in the same conditions to compare the values of hardness and fracture toughness with those of FGM. In addition, the FGM samples for flexural strength test were produced, the characteristics of which will be mentioned in the following sections.

2.3. Sample characterisation and machining test

Samples of each FGM (Al_2O_3–ZrO_2 + WC-Co and Al_2O_3–TiC + WC-Co) were sectioned using a precision saw (IsoMet 4000) and a diamond wheel 15HC for metallographic analysis. Subsequently, they were mounted in a phenolic thermoset resin using a SimpliMet 3000 machine. The samples were ground manually using SiC powders with grit sizes of 400, 600, and 1000. Then, they were polished using Nylon PSA cloths with diamond pastes (MetaDi II) having particle sizes of 15, 6, and 1 μm. The machines and consumables were made by Buehler. The microscopic analyses were performed using a scanning electron microscope (model TM3000 by Hitachi).

Table 2
Alumina and cemented carbide volume fractions for the FGMs.

Layers	Volume fraction [%]	
	Al_2O_3–ZrO_2 or Al_2O_3–TiC	WC-Co
1	100	–
2	86	14
3	79	21
4	72	28
5	58	42
6	44	66

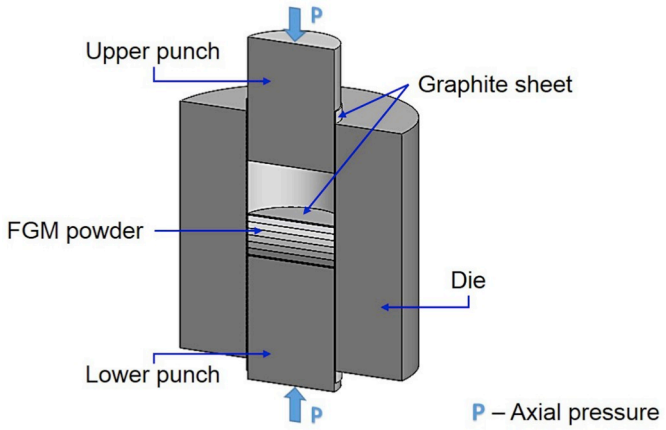

Fig. 1. Sintering die assembly.

The relative densities were assessed using Archimedes' principle (precision scale, 200 CE by Marte, and hydrostatic kit). Hence, a series of mass measurements based on ISO 10545–3:2018 [22] were performed to determine the experimental densities (ρ_{exp}), as shown in Eq. (5):

$$\rho_{exp} = \frac{m_1}{m_2 - m_3}\rho_{H_2O} \quad (5)$$

where m_1 is the mass of the dry samples, m_2 is the mass of the samples impregnated with water, and m_3 is the mass of the samples while suspended in water.

The distilled water density was determined by $\rho_{H_2O} = 1.0017 - 0.0002135T$ [g/cm^3], in which T is the water temperature in [°C], measured using a spit type digital thermometer (model TM879 by Equitherm).

According to German and Park [23], the theoretical density (ρ_t) can be obtained using the mixtures rule, as shown in Eq. (6):

$$\frac{1}{\rho_t} = \frac{wt\%_{ceramic}}{\rho_{ceramic}} + \frac{wt\%_{cemented}}{\rho_{cemented}} \quad (6)$$

The powders manufacturer data sheets were used to determine the ceramics ($\rho_{ceramic}$) and cemented carbide ($\rho_{cemented}$) densities. $wt\%$ denotes the weight percentage used for ceramic (Al_2O_3–ZrO_2 or Al_2O_3–TiC) and cemented carbide (WC–Co).

Vickers indentation hardness tests were conducted in homogeneous Al_2O_3–ZrO_2 and Al_2O_3–TiC samples and on the first layer of the FGM tools, i.e., on the Al_2O_3–ZrO_2 and Al_2O_3–TiC layers, to compare the material resistances to penetration (mechanical property) with sintering features and thermal residual stress. This layer is important because it will be in contact with the workpiece during machining; hence, it must be harder and consequently resist wear. The tests were conducted according to ASTM C1327-15 [24] in metallographically prepared samples. The hardness tester used was a Vickers VMT-7 by Buehler. We evaluated 10 indentations with loads (P) of 5 kgf for each sample. The Vickers hardness number was computed in gigapascals, using P in Newtons and surface-projected diagonals length (d) in millimetres, as shown in Eq. (7).

$$HV = 0.0018544\left(\frac{P}{d^2}\right) \quad (7)$$

Fracture toughness, which is the force required to extend a crack through the microstructure, was measured using the Vickers indentation hardness test aforementioned. Equation (8) was used to calculate the plain-strain fracture toughness (K_{IC}) in mode I of loading [25].

$$K_{IC} = 0.0016\left(\frac{E}{H}\right)^{1/2}\frac{P}{c^{3/2}} \quad (8)$$

where E is the elasticity modulus [GPa], H is the hardness value [GPa], P is the load applied [N], c is the crack extension [m], and K_{IC} is given [MPa.m$^{1/2}$]. P was adjusted such that c was larger than the average length of diagonal impressions.

The flexural strength test, which measures the ultimate strength in bending, was performed at ambient temperature from an adaptation of ASTM C1161-02c:2008 [26]. The samples dimensions were 25 mm in length, 4 mm in width, and 6 mm in thickness. Previously, they were sintered by SPS with dimension of 25 × 13 × 6 mm at 50 MPa (due to graphite die resistance limitation), temperature of 1300 °C and a dwell time of 5 min. Subsequently, the samples were sectioned using a precision saw machine, as previously mentioned. Homogeneous ceramics and FGM samples were tested as fabricated, i.e., the faces were not ground. The tests were conducted in a universal test machine (model Sintech 5/G by MTS). Three-point loadings with a support spans of 20 mm and a crosshead speed of 0.5 mm/min were used to evaluate the samples. Five workpieces were tested for each sample.

The machining test was performed without following ceramic cutting tool standards, simply to explore the capabilities of FGM cutting tools. A conventional lathe (Romi S30 of 8 HP) was used as tool-machine. The workpiece material was martensitic stainless steel (VSM 13 by Villares Metals) with 276.4 HV30. New rounded FGM samples were sintered and sectioned in a square form by using the precision saw machine to obtain a geometry as close as possible to that of SNGN 120716. The FGM cutting tools were assembled in a tool-holder (CSRNR 2525 M12-4 by Sandvik), permitting a cutting geometry with a cutting edge inclination angle of −6°, clearance angle (α) of 6°, rake angle (γ) of −6°, and cutting edge angle (k_r) of 75°. The cutting conditions were kept constant at v_c = 100 m/min (cutting speed), f = 0.205 mm/rev (feed rate), and a_p = 2 mm (depth of cut). The feed length was 10 mm. The main cutting force was monitored with the aid of a piezoelectric dynamometer, model 9265B/9441B, using a signal amplifier 5070A 11100 and the acquisition software DynoWare 2825A1-2 by Kistler. The dynamometer was assembled on the lathe tool-holder. After that, the FGM cutting tools were brought to TM3000, scanning electron microscope, to be evaluated. Ra (arithmetic average height) and Rz (mean of maximum peak to valley height) roughness parameters were evaluated by a roughness tester, SJ-201P by Mitutoyo, with cut-off set at 0.8 mm, according to ISO 4288:1996 [27].

3. Results and discussion

3.1. Thermal residual stress and microscopy

Fig. 2 shows the thermal residual stresses estimated at the centre of the FGM AlZr and FGM AlTiC layers. Pastor et al. [28] obtained 1.13 GPa of ultimate strength for Al_2O_3–ZrO_2(3.5 mol%Y_2O_3) with a volume ratio of 30%ZrO_2. Deng et al. [29] sintered Al_2O_3–TiC (50 vol %TiC) and obtained 0.80 GPa of strength. From the literature cited, note that the estimated stresses are lower than those of the ultimate strengths for parts in approximate conditions. Theoretically, from this analysis, it is supposed that none of the FGM elements exhibit flaws, such as cracking or delamination, after sintering.

Fig. 3 shows an SEM assembly of FGM structures, in which six layers can be observed. The first one is only an alumina composite and the last one is richer in cemented carbide. Based on the microscopic analysis, no crack was observed, and it was concluded that the thermal residual stress model used was appropriate for tailoring such FGM structures. However, agglomerates, dark and white spots are present in the microstructure, due to the inaccurate conditions during powder-mixing.

The first two layers of each FGM are depicted in Fig. 4. These layers are the most important owing to their residual stress level being larger than that of the other layers, according to the estimation shown in Fig. 1. EDS maps aid in clarifying that the lack of perpendicular cracks and delamination between layers must occur due to the continuity of the constituents from one layer to the other in a gradient form; this causes stress mismatch, thereby keeping the stresses lower than the fracture strength of the most brittle material. As observed by Ravichandran [20], the higher the number of layers, the lower the residual stress levels. If not, cracks are observed to arise, as noted by Gillia; Caillens [11]. Kawasaki and Watanabe [7] also state that particle size, thermal expansion coefficient differences, difference in the layers thickness and uniformity mixing of powders are factors that make an FGM structure effective.

3.2. Physical and mechanical characterisation

Table 3 details the relative density results for the two sintered FGMs.

Sintering through SPS provides an elevated relative density level with lower sintering temperature and shorter holding time when compared to those of conventional methods. The results indicated fully dense samples after the thermal treatment, in accordance with the literature; however, in Fig. 4, we can still see some nanometric pores in the first layer, which is rich in alumina and faces greater difficulty in reaching full densification. Tuan et al. [30] sintered Al_2O_3–ZrO_2 with a particle size of approximately 0.20 μm and external pressure of 30 MPa at 1350 °C for 5 min. Zhang et al. [31] sintered Al_2O_3–TiC with a particle size of approximately 0.30 μm at 50 MPa and 1480 °C for 4 min. Santanach et al. [32] sintered α-Al_2O_3 with a particle size of 0.14 μm at 100 MPa and 1300 °C for 5 min. In all cases, the authors performed sintering using SPS and obtained a relative density exceeding 99%, without abnormal growth grain. For cemented carbide, Cha et al. [33] sintered WC-10Co with a particle size of 1.33 μm under a pressure of 50 MPa at 1110 °C for 10 min. Shi et al. [34] sintered nanometric WC-6Co powder at 50 MPa and 1100 °C for 10 min. Huang et al. [35] sintered WC-6Co powder with a particle size of approximately 1.4 μm at 45 MPa and 1250 °C for 5 min. The cited authors used SPS to provide the heat treatment and obtained nearly full densification. The cemented carbide sintering via SPS generally occurs with liquid phase formation around 1000 °C; consequently, there is a reduction in the surface free energy that drives the densification. Therefore, the cemented carbide phase is expected to reach full densification before alumina under the sintering conditions tested.

Table 4 presents the hardness and fracture toughness results for homogeneous ceramics (Al_2O_3–ZrO_2 and Al_2O_3–TiC) and for FGM first layers (Al_2O_3–ZrO_2 and Al_2O_3–TiC layers). The confidence intervals (CI) of 95% were added to support the comparison. The ceramic layers remain in contact with the workpiece during machining, forming the chip-tool interface; hence, it is important to evaluate the hardness and calculate their resistance to crack propagation. In addition, values of WC-Co were extracted from the literature for a comprehensive comparative analysis.

The hardness value for Al_2O_3–ZrO_2 is nearly 5% higher than the first layer of FGM AlZr. This difference is statistically significant for a 5% significance level. It may be associated with the thermal residual stress present in the first layer of FGM. The fracture toughness results follow the same tendency; however, a significant difference was not noted. The hardness and fracture toughness results for Al_2O_3–ZrO_2 are close to those in the literature. Pastor et al. [28] obtained values of 15.3 GPa and 4.8 MPa m$^{1/2}$, respectively. Meng et al. [36], using the SPS technique, obtained 18 GPa and 5.1 MPa m$^{1/2}$, respectively. Ezugwu and

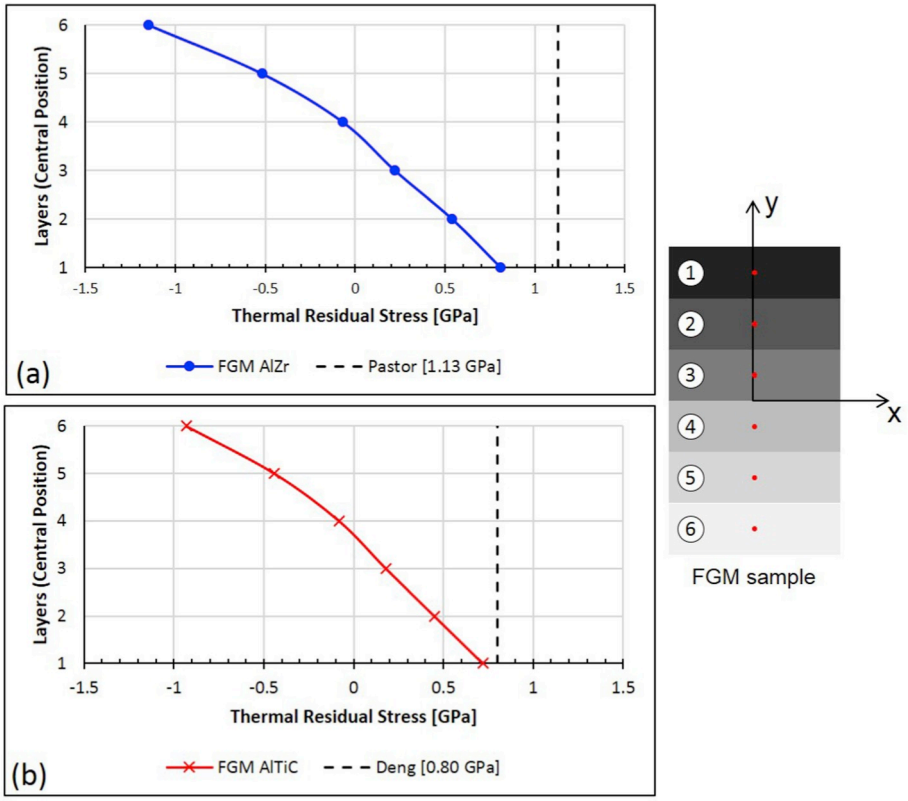

Fig. 2. Estimated thermal residual stress. (a) FGM Al_2O_3–ZrO_2 + WC-Co; (b) FGM Al_2O_3–TiC + WC-Co.

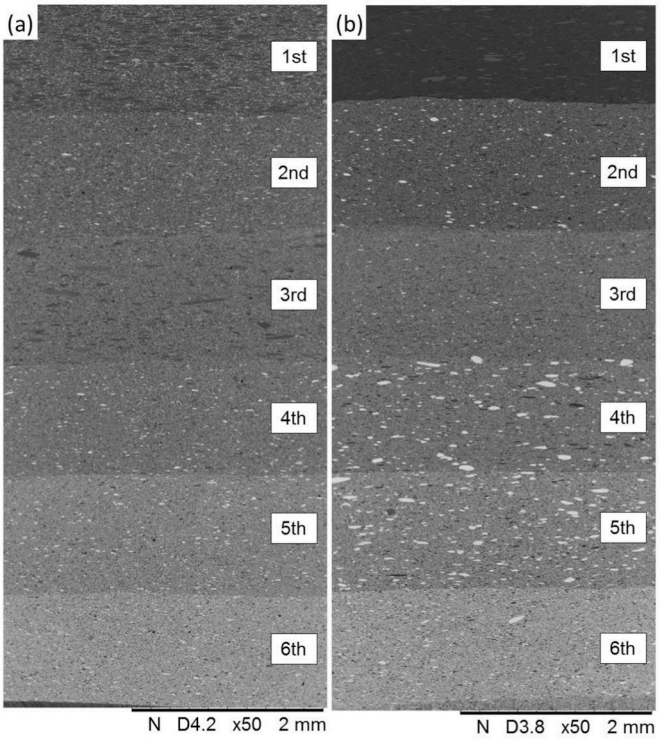

Fig. 3. SEM microscopic characterisation of FGMs structures.
(a) FGM Al_2O_3–ZrO_2 + WC-Co; (b) FGM Al_2O_3–TiC + WC-Co.

Tang [37] reported hardness and fracture toughness values of 18 GPa and 4.3 MPa $m^{1/2}$ for the Al_2O_3–ZrO_2 cutting tool, respectively. The variation among the results is associated with different ZrO_2 contents, sintering parameters, and powder processing techniques. The hardness value for homogeneous Al_2O_3–TiC is around 3% higher than the Al_2O_3–TiC layer of FGM. Nevertheless, there was no significant difference observed. The K_{IC} values show the same data behaviour. For Al_2O_3–TiC, the hardness value was slightly below expectations. Xu et al. [38] obtained 19.1 GPa and 4.92 MPa $m^{1/2}$ for hardness and fracture toughness, respectively. Deng et al. [29] obtained 20 GPa and 5.2 MPa $m^{1/2}$, respectively. Zhang et al. [31], by using SPS, achieved 21 GPa and 3.87 MPa $m^{1/2}$, respectively. The cause of the lower value of hardness may be the free carbon content in the alumina matrix from TiC and graphite sheet, as well as failing to prepare homogenised powder mixtures properly and the lack of additional thermal support. In general, the sintering conditions chosen were satisfactory for the results of the observed mechanical properties. It is worth stressing that the comparison of hardness and fracture toughness between ceramic samples is important to evaluate the thermal residual stress behaviour of FGMs. The results showed values a little higher for homogenous ceramics. This may mean that the thermal residual stress model may be overestimating the output values or the sintering system used was able to reduce the residual stress. The hardness and fracture toughness values presented for cemented carbide are averages extracted from Upadhyaya [39], 15.5 GPa and 9.6 MPa $m^{1/2}$; Raihanuzzaman et al. [40], 15 GPa and 12.4 MPa $m^{1/2}$ and Huang et al. [35], 17.3 GPa and 13.9 MPa $m^{1/2}$. As Trent and Wright [14] mentioned, at room temperature (20–25 °C), the hardness of alumina-based ceramics is close to that of cemented carbides; however, the former retains their mechanical properties at higher temperatures, allowing higher cutting speeds. Moreover, alumina is almost inert in steel up to its melting point. However, the lower toughness of homogeneous ceramics hinders their wider application as cutting tools.

Fig. 5 presents results of flexural strength for homogenous ceramics and their respective FGMs. From the literature, an average value for cemented carbide (WC–6Co) was also included for comparison. The flexural strength for FGM AlZr was approximately 50% higher than homogenous Al_2O_3–ZrO_2, while FGM AlTiC was 137% higher than Al_2O_3–TiC. The

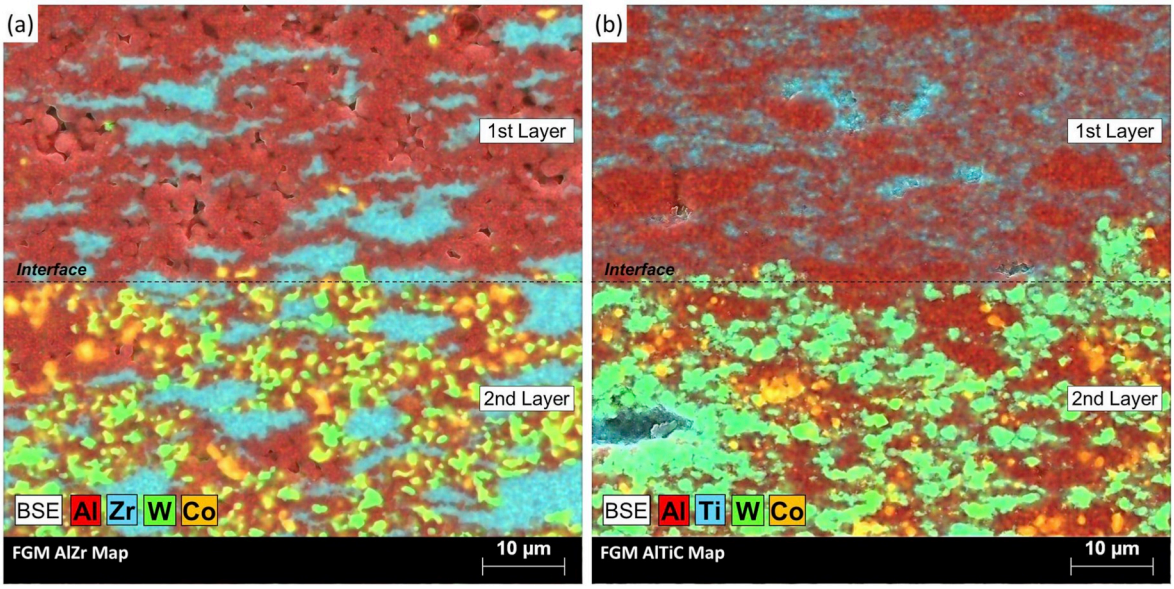

Fig. 4. EDS maps characterising the interface of the first and second layers. (a) FGM Al_2O_3–ZrO_2 + WC-Co; (b) FGM Al_2O_3–TiC + WC-Co.

Table 3
Relative density of FGMs sintered.

Sintering conditions 1300 °C; 70 MPa; 5 min	
FGM AlZr	FGM AlTiC
100%	99.65%

values found, mainly for homogeneous ceramics, are lower than those presented in the literature. Pastor et al. [28] obtained 1130 MPa of flexural strength for Al_2O_3-30 vol%ZrO_2 produced by pressureless sintering and directional solidification using the laser-heated float zone method. Liu et al. [41] found values between 621 and 791 MPa for Al_2O_3-15 vol%ZrO_2 prepared by gelcasting process and sintered. Tuan et al. [30] obtained 895 MPa for Al_2O_3-5 vol%ZrO_2 sintered by pulse electric current. In relation to homogenous Al_2O_3–TiC, Cutller and Hurford [42] found flexural strength between 469 and 595 MPa, varying according to carbon content, for hot-pressed Al_2O_3-25 vol%TiC. Xu et al. [38] obtained values between 782 and 817 MPa, when studying volume fraction of free carbon content in hot pressed Al_2O_3-30 vol%TiC. Deng et al. [29] obtained 800 MPa for hot-pressed Al_2O_3-50 vol%TiC. The difference between the results presented in this paper and the one in the literature may be related to more sophisticated powder preparation in favour of the latter, when they used chemical products to improve the constituents' dispersion. Moreover, the samples were tested as manufactured, i.e., the faces were not ground, hence surface defects, such as microcracks that can propagate toward the bulk may harm the mechanical property. Finally, SPS sintering is characterised by the use of graphite sheet wrapping the powder and graphite die. Both are sources of carbon, as noted by Xu et al. [38]. With the increase in the volume fraction of free carbon, the flexural strength tends to decrease. However, the most important observation is that the FGMs could greatly improve the flexural strength, retaining an intermediate position between the homogenous ceramics and cemented carbide. Consequently, the application field of ceramics can be extended. The higher the content of ductile constituent, the closer the structured part is achieving the toughness behaviour. Note that it is important to ensure gradient continuity to avoid cracks due to residual stress. In this case, cemented carbide (WC–6Co) is the most ductile constituent. Its flexural strength value was obtained from an average in Ezugwu and Pashby [43] that reached 2000 MPa; Upadhyaya [39] also attained a value of 2000 MPa; Shi et al. [34] obtained value of 1220 MPa sintering by SPS and 1800 MPa by vacuum sintering, and Zhang et al. [44] obtained a value of 2300 MPa.

3.3. Machining evaluation

Fig. 6 presents the cutting force values for the FGM tools, which machined martensitic stainless steel (276.4 HV30) in a conventional lathe. The FGM AlZr and FGM AlTiC supported 965 and 1065 N of main cutting forces, respectively, without any catastrophic failure. Kumar et al. [45] obtained approximately 475 and 525 N when turning EN 24 steel with 392 and 446 HV, respectively, using a commercially mixed alumina ceramic cutting tool at a cutting speed of 120 m/min, feed rate of 0.12 mm/rev and a depth of cut of 0.5 mm. Kumar and Patel [46] found the cutting force to be approximately 375 N when turning AISI 52100 steel with 746 HV, using an uncoated mixed ceramic tool at 110 m/min, 0.2 mm/rev and 0.5 mm. In Fig. 6, when machining with an uncoated cemented carbide cutting tool (TPUN 160304) in an orthogonal geometry (tool-holder CTGPR 2525 M 16) with the same workpiece material and cutting conditions, a similar cutting force of approximately 1000 N was found. The aforementioned results aid in justifying the viability of the proposed cutting tool materials, as the machining tests with FGMs tools were performed out of the standards,

Table 4
Results of hardness and fracture toughness.

	Hardness [GPa]	± 95%CI [GPa]	K_{IC} [MPa.m$^{1/2}$]	± 95%CI [MPa.m$^{1/2}$]
Al_2O_3–ZrO_2	17.22 ± 0.51	16.75–17.70	5.17 ± 0.56	4.65–5.69
Al_2O_3–ZrO_2 layer	16.38 ± 0.51	16.02–16.75	4.76 ± 0.44	4.44–5.08
Al_2O_3–TiC	16.83 ± 0.96	16.15–17.52	4.59 ± 0.69	4.00–5.17
Al_2O_3–TiC layer	16.29 ± 0.83	15.69–16.89	4.54 ± 0.45	4.21–4.86
WC-Co averages [35,39,40]	15.93 ± 1.21	12.93–18.94	11.97 ± 2.18	6.55–17.39

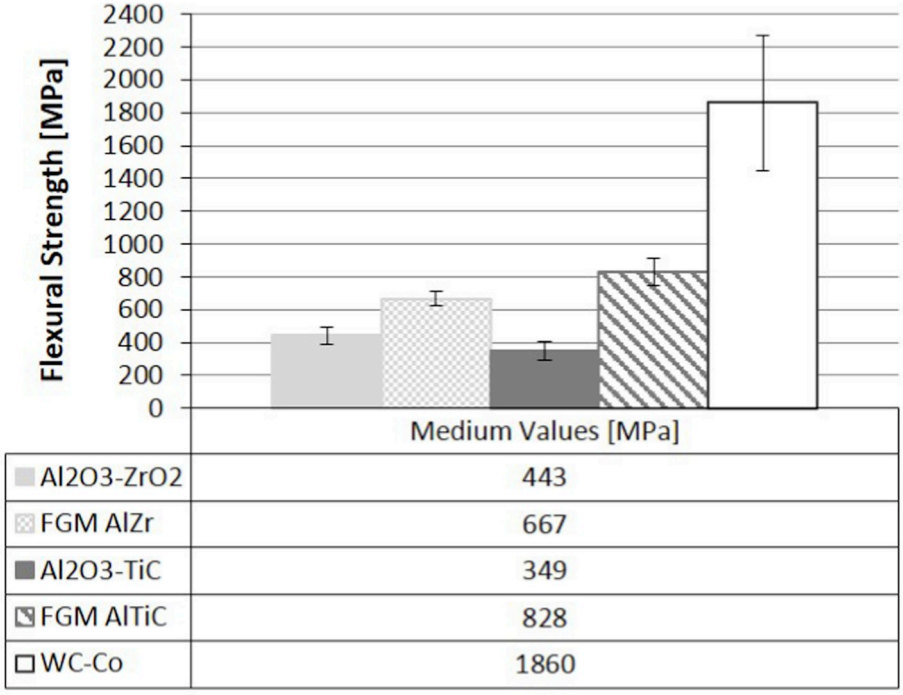

	Medium Values [MPa]
Al2O3-ZrO2	443
FGM AlZr	667
Al2O3-TiC	349
FGM AlTiC	828
WC-Co	1860

Fig. 5. Flexural strength comparison between the homogeneous ceramics, FGMs and WC-Co.

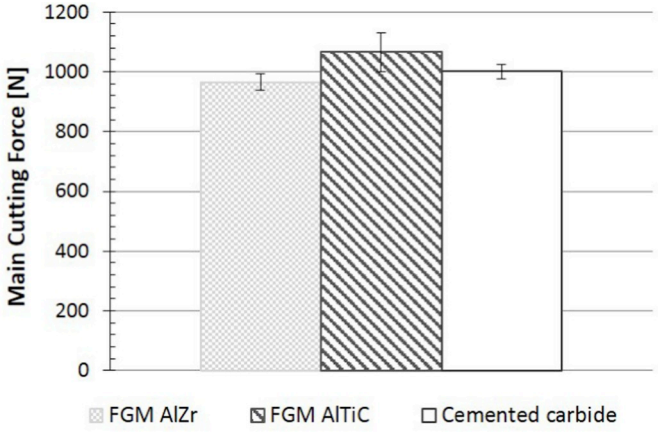

Fig. 6. Results of cutting force for turning martensitic stainless steel at a cutting speed of 100 m/min, feed rate of 0.205 mm/rev, and a depth of cut of 2 mm.

i.e., in a conventional lathe, without sufficient stiffness, and machining a ductile workpiece material, although its microstructure was martensitic. Conversely, as previously mentioned, it is important to note that improvements in all the powder metallurgy processes are still necessary, which implies that the obtained results can still be improved.

Table 5 presents the workpiece surface roughness results. For the FGM AlZr and FGM AlTiC tools, the arithmetic average height (Ra) parameter values were 1.49 and 2.88 μm, respectively. Regarding, the average of the highest peaks and lowest valleys (Rz) obtained from the five sampling lengths within the assessment length, the AlZr and AlTiC FGMs obtained 7.67 and 13.09 μm, respectively. The difference between the values can be attributed to the slight differences in the tool tip, which is a result of manufacturing limitations. Although the faces and edges of the FGM cutting tools were not properly ground, the roughness results for both the evaluated parameters were comparable to the ones in the literature in which commercial cutting tools were used. Kumar et al. [45] turned EN-24 steel (~446 HV) at 120 m/min, 0.12 mm/rev and 0.5 mm with cutting tools made of mixed alumina ceramic and zirconia-toughened alumina ceramic having a cutting tool geometry similar to the ones used in this study. They obtained the following values of surface roughness for the Ra parameter: approximately 6.5 μm for the former tool, and 7 μm for the latter. Kumar and Patel [46] evaluated the surface finishing of AISI 52100 steel (~746 HV), turned by Al_2O_3–TiCN mixed ceramic tools. They found the values to be approximately 2.5 μm for Ra in approximate cutting conditions of 110 m/min, 0.2 mm/rev, and 0.5 mm and with a similar cutting tool geometry. Das et al. [47] turned EN-24 alloy steel (~484 HV) using a coated cermet tool with similar cutting tool geometry. At cutting conditions of 150 m/min, 0.17 mm/rev and 0.8 mm, they found values of surface roughness of 3.5 and 18.9 μm for Ra and Rz, respectively.

Table 5
Results of surface roughness.

	Ra [μm]	Rz [μm]
FGM AlZr	1.49 ± 0.11	7.67 ± 1.29
FGM AlTiC	2.88 ± 0.44	13.09 ± 2.40

The wear mechanisms in ceramic cutting tools include abrasion, fracture, adhesion (attrition), and diffusion due to high cutting speeds and, consequently, high temperatures developed on the rake face and clearance face. As for the types of tool wear, flank wear is observed on the clearance face due to the abrasion wear mechanism. This type of wear occurs due to hard particles that can be embedded on a surface sliding on a counterface (two-body abrasion) or free to roll and slide (three-body abrasion) between two surfaces. The wear appears in the form of parallel grooves in the direction of the chip or workpiece flow. Crater wear can be seen when the cutting temperature is extremely high and chemical affinity is present between the workpiece and tool. In this case, diffusion mechanism is present in some ceramics, such as alumina whiskers and Si_3N_4, when they are used for machining steel. The wear, in this case, appears as a smooth crater on the rake face, although it can also be seen on the flank. Notch wear usually occurs in machining materials that tend to strain hardening. It is characterised as a groove formed at the free edge of the chip on the main cutting edge. A temperature difference is observed among the extremities and the center of chip during its formation, which implies that there is more deformation

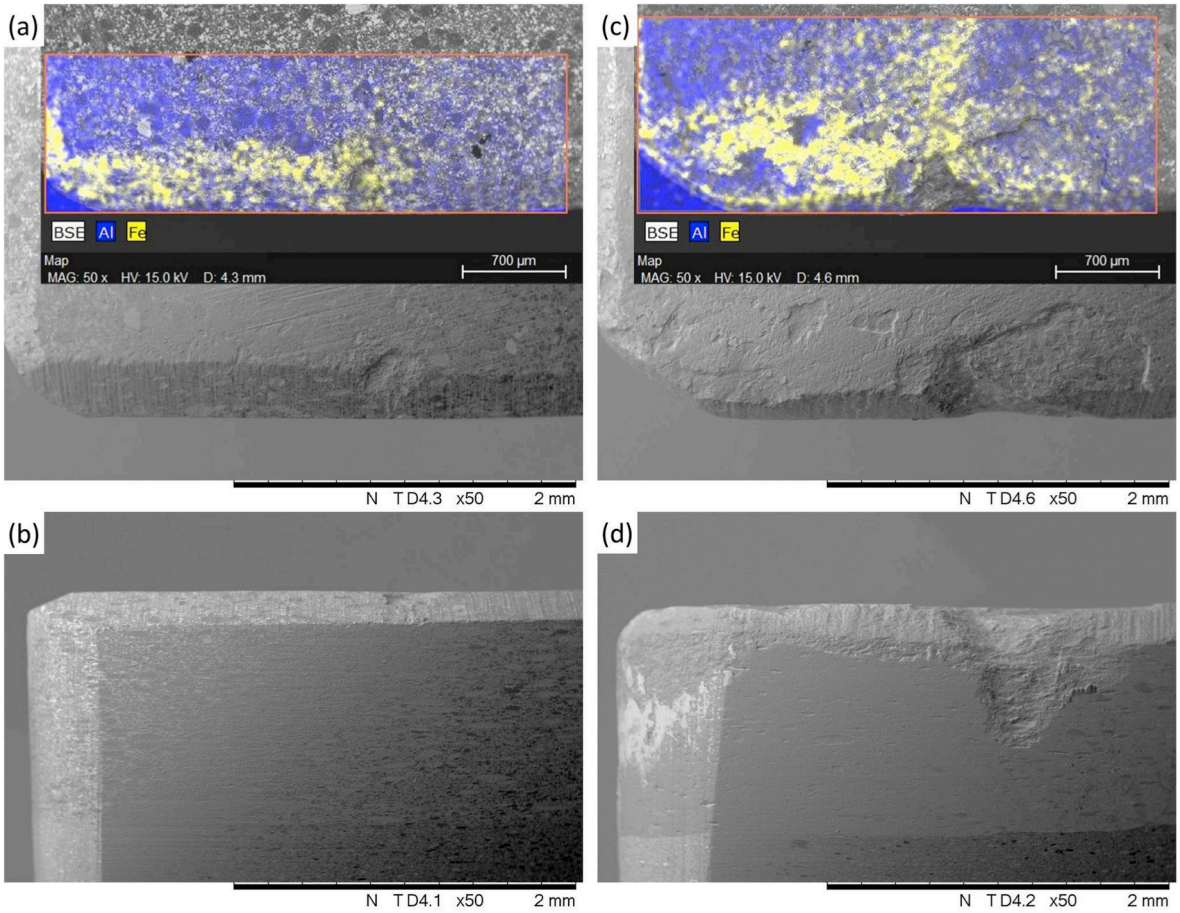

Fig. 7. SEM images of wear for FGM tools. (a) Rake face of FGM AlZr with EDS highlighting workpiece material adhesion; (b) Tool flank of FGM AlZr with small spalling on the main cutting edge; (c) Rake face of FGM AlTiC with EDS highlighting adhesion and large spalling; (d) Tool flank of FGM AlTiC with notch wear presence.

energy in the extremities; this also suggests fatigue due to force fluctuation and thermal crack formation. Furthermore, at the perimeter of contact on the main cutting edge where the groove is formed there is atmosphere presence, causing abrasive oxide layer adhesion, consequently generating attrition wear mechanism. Fig. 7 shows SEM images of FGM cutting tools. The rake faces of FGM AlZr and FGM AlTiC are depicted in Fig. 7 (a) and (c), respectively. A small spalling is verified on the main cutting edge for FGM AlZr and a large one, notch wear formation, for FGM AlTiC. Additionally, the adhesion of martensitic stainless steel (workpiece material) on the tool rake face is also observed, as highlighted in the EDS picture. When the tool flank (clearance face) is analysed, as shown in Fig. 7 (b) and (d), large signals of abrasion wear mechanism are not observed for any of the cutting tools owing to the short machining period. Instead, an intense and distinguished notch wear is observed for FGM AlTiC, which may have occurred due to the elevated free carbon content or failure in the powder preparation. Kumar et al. [45] observed flank, crater and notch wear turning EN-24 steel (446 HV) with mixed alumina ceramic and zirconia-toughened alumina ceramic cutting tools. They noted abrasion, adhesion and diffusion as wear mechanisms. Kumar et al. [48] observed flank, crater and notch wear for mixed alumina ceramic and whisker reinforced alumina ceramic cutting tools turning martensitic stainless steel (697 HV) and EN-24 hardened steel (446 HV). Corrêa et al. [49] turned similar material (martensitic, ~173 HV, and supermartensitic stainless steel, ~290 HV, S41000 and S41426) using coated cemented carbide, in the same cutting conditions as the ones in this study, although they used vegetable-based cutting fluid. They observed abrasion, adhesion (attrition), and spalling as wear mechanisms, which caused flank and notch wear. Kumar and Patel [46] observed abrasion and adhesion as wear mechanisms in a mixed ceramic cutting tool that generated flank wear and spalling, when turning AISI 52100 (746 HV).

4. Conclusions

Microstructure analysis showed the parts of the FGM without cracks. This justifies the importance of evaluating the volume fraction of constituents from residual stress models in advance. In addition, the effectiveness of the FGM is determined by the constituents' continuity in the graded direction. The SPS technique was able to sinter dense FGM elements. The hardness and toughness values were close to those in the literature, except for the Al_2O_3–TiC layer. The most important result showed that the FGMs can significantly improve the flexural strength values; and, consequently, the application field of ceramics can be extended. The main cutting force values suggest the FGM inserts are resistant; they could support elevated loading (around 1000 N), even when operating in a conventional lathe without sufficient stiffness. Although the faces and edges of the FGMs were not properly ground, the roughness results (Ra and Rz parameters) were comparable to those in the literature in which commercial cutting tools were used. From the wear analysis, a small spalling was observed on the main cutting edge for FGM AlZr, notch wear formation for FGM AlTiC, in addition to the adhesion of the workpiece material on the rake face of both the cutting tools.

Declaration of competing interest

The authors declare that they have no known competing financial interests or personal relationships that could have appeared to influence the work reported in this paper.

Acknowledgments

The authors would like to thank FAPESP (Grants 2010/00683-2), CNPq (Grants 472145/2010-0; 405707/2013-4), Capes, FAPES (Grant 083/2019) for providing financial support and Villares Metals S.A. for donating the workpiece.

References

[1] K. Yang, W.-Z. Feng, H.-F. Peng, J. Lv, A new analytical approach of functionally graded material structures for thermal stress BEM analysis, Int. Commun. Heat Mass Tran. 62 (2015) 26–32, https://doi.org/10.1016/J.ICHEATMASSTRANSFER.2015.01.009.

[2] Y. Miyamoto, W. Kaisser, B.H. Rabin, A. Kawasaki, R.G. Ford, Functionally Graded Materials : Design, Processing, and Applications, Springer Science & Business Media, New York, 1999.

[3] M. Mott, J.R. Evans, Zirconia/alumina functionally graded material made by ceramic ink jet printing, Mater. Sci. Eng. 271 (1999) 344–352, https://doi.org/10.1016/S0921-5093(99)00266-X.

[4] Y. Watanabe, H. Sato, Review fabrication of functionally graded materials under a centrifugal force, in: D.J. Cuppoletti (Ed.), Nanocomposites with Unique Prop. Appl. Med. Ind, InTech, 2011, p. 360, , https://doi.org/10.5772/20988.

[5] G. Udupa, S.S. Rao, K.V. Gangadharan, Functionally graded composite materials: an overview, Procedia Mater. Sci. 5 (2014) 1291–1299, https://doi.org/10.1016/J.MSPRO.2014.07.442.

[6] M. Naebe, K. Shirvanimoghaddam, Functionally graded materials: a review of fabrication and properties, Appl. Mater. Today. 5 (2016) 223–245, https://doi.org/10.1016/J.APMT.2016.10.001.

[7] A. Kawasaki, R. Watanabe, Concept and P/M fabrication of functionally gradient materials, Ceram. Int. 23 (1997) 73–83, https://doi.org/10.1016/0272-8842(95)00143-3.

[8] M.R. Murshed, S.I. Ranganathan, F.H. Abed, Design maps for fracture resistant functionally graded materials, Eur. J. Mech. Solid. 58 (2016) 31–41, https://doi.org/10.1016/j.euromechsol.2016.01.002.

[9] J. Ma, G.E. Tan, Processing and characterization of metal–ceramics functionally gradient materials, J. Mater. Process. Technol. 113 (2001) 446–449, https://doi.org/10.1016/S0924-0136(01)00613-6.

[10] M.A. Meyers, K.K. Chawla, Mechanical Behavior of Materials, Cambridge University Press, New York, 2009.

[11] O. Gillia, B. Caillens, Fabrication of a material with composition gradient for metal/ceramic assembly, Powder Technol. 208 (2011) 355–366, https://doi.org/10.1016/J.POWTEC.2010.08.029.

[12] M. Tokita, Mechanism of spark plasma sintering, Proc. 2000 Powder Metall. World Congr. 2001, pp. 729–732.

[13] R. Orrù, R. Licheri, A.M. Locci, A. Cincotti, G. Cao, Consolidation/synthesis of materials by electric current activated/assisted sintering, Mater. Sci. Eng. R Rep. 63 (2009) 127–287, https://doi.org/10.1016/J.MSER.2008.09.003.

[14] E. Trent, P.K. Wright, Metal Cutting, fourth ed., Butterworth-Heinemann, Boston, 2000.

[15] Z. Jun, A. Xing, D. Jianxin, W. Jinghai, Thermal shock behaviors of functionally graded ceramic tool materials, J. Eur. Ceram. Soc. 24 (2004) 847–854, https://doi.org/10.1016/S0955-2219(03)00315-7.

[16] F. Gong, J. Zhao, Z. Li, J. Sun, X. Ni, G. Hou, Design, fabrication and mechanical properties of multidimensional graded ceramic tool materials, Ceram. Int. 44 (2018) 2941–2951, https://doi.org/10.1016/J.CERAMINT.2017.11.046.

[17] W. Lengauer, K. Dreyer, Functionally graded hardmetals, J. Alloys Compd. 338 (2002) 194–212, https://doi.org/10.1016/S0925-8388(02)00232-3.

[18] W. Ji, B. Zou, S. Zhang, H. Xing, H. Yun, Y. Wang, Design and fabrication of gradient cermet composite cutting tool, and its cutting performance, J. Alloys Compd. 732 (2018) 25–31, https://doi.org/10.1016/J.JALLCOM.2017.10.187.

[19] A. Xing, Z. Jun, H. Chuanzhen, Z. Jianhua, Development of an advanced ceramic tool material—functionally gradient cutting ceramics, Mater. Sci. Eng. 248 (1998) 125–131, https://doi.org/10.1016/S0921-5093(98)00502-4.

[20] K.S. Ravichandran, Thermal residual stresses in a functionally graded material system, Mater. Sci. Eng. 201 (1995) 269–276, https://doi.org/10.1016/0921-5093(95)09773-2.

[21] W. Lanhe, Thermal buckling of a simply supported moderately thick rectangular FGM plate, Compos. Struct. 64 (2004) 211–218, https://doi.org/10.1016/J.COMPSTRUCT.2003.08.004.

[22] Iso, ISO 10545-3:2018 - Ceramic Tiles - Part 3: Determination of Water Absorption, Apparent Porosity, Apparent Relative Density and Bulk Density, (2018).

[23] R.M. German, S.J. Park, Mathematical Relations in Particulate Materials Processing : Ceramics, Powder Metals, Cermets, Carbides, Hard Materials, and Minerals, John Wiley & Sons, 2008.

[24] Astm International, ASTM C1327 - 15 Standard Test Method for Vickers Indentation Hardness of Advanced Ceramics, (2015), https://doi.org/10.1520/C1327-15.

[25] G.R. Anstis, P. Chantikul, B.R. Lawn, D.B. Marshall, A critical evaluation of indentation techniques for measuring fracture toughness: I, direct crack measurements, J. Am. Ceram. Soc. 64 (1981) 533–538, https://doi.org/10.1111/j.1151-2916.1981.tb10320.x.

[26] Astm International, ASTM C1161 - 02c Standard Test Method for Flexural Strength of Advanced Ceramics at Ambient Temperature, (2008), https://doi.org/10.1520/C1161-02CR08E01.

[27] Iso, ISO 4288:1996 - Geometrical Product Specifications (GPS) - Surface Texture: Profile Method - Rules and Procedures for the Assessment of Surface Texture, (1996).

[28] J.Y. Pastor, P. Poza, J. LLorca, J.I. Peña, R.I. Merino, V.M. Orera, Mechanical properties of directionally solidified Al2O3–ZrO2(Y2O3) eutectics, Mater. Sci. Eng. 308 (2001) 241–249, https://doi.org/10.1016/S0921-5093(00)02040-2.

[29] J. Deng, T. Can, J. Sun, Microstructure and mechanical properties of hot-pressed Al2O3/TiC ceramic composites with the additions of solid lubricants, Ceram. Int. 31 (2005) 249–256, https://doi.org/10.1016/J.CERAMINT.2004.05.009.

[30] W.H. Tuan, S.M. Liu, C.J. Ho, C.S. Lin, T.J. Yang, D.M. Zhang, Z.Y. Fu, J.K. Guo, Preparation of Al2O3–ZrO2–Ni nanocomposite by pulse electric current and pressureless sintering, J. Eur. Ceram. Soc. 25 (2005) 3125–3133, https://doi.org/10.1016/J.JEURCERAMSOC.2004.07.001.

[31] Y. Zhang, L. Wang, W. Jiang, L. Chen, G. Bai, Microstructure and properties of Al2O3–TiC nanocomposites fabricated by spark plasma sintering from high-energy ball milled reactants, J. Eur. Ceram. Soc. 26 (2006) 3393–3397, https://doi.org/10.1016/J.JEURCERAMSOC.2005.09.036.

[32] J.G. Santanach, A. Weibel, C. Estournès, Q. Yang, C. Laurent, A. Peigney, Spark plasma sintering of alumina: study of parameters, formal sintering analysis and hypotheses on the mechanism(s) involved in densification and grain growth, Acta Mater. 59 (2011) 1400–1408, https://doi.org/10.1016/J.ACTAMAT.2010.11.002.

[33] S.I. Cha, S.H. Hong, B.K. Kim, Spark plasma sintering behavior of nanocrystalline WC–10Co cemented carbide powders, Mater. Sci. Eng. 351 (2003) 31–38, https://doi.org/10.1016/S0921-5093(02)00605-6.

[34] X.L. Shi, G.Q. Shao, X.L. Duan, R.Z. Yuan, H.H. Lin, Mechanical properties, phases and microstructure of ultrafine hardmetals prepared by WC–6.29Co nanocrystalline composite powder, Mater. Sci. Eng. 392 (2005) 335–339, https://doi.org/10.1016/J.MSEA.2004.09.043.

[35] Z. Huang, X. Ren, M. Liu, C. Xu, X. Zhang, S. Guo, H. Chen, Effect of Cu on the microstructures and properties of WC-6Co cemented carbides fabricated by SPS, Int. J. Refract. Metals Hard Mater. 62 (2017) 155–160, https://doi.org/10.1016/J.IJRMHM.2016.06.007.

[36] F. Meng, C. Liu, F. Zhang, Z. Tian, W. Huang, Densification and mechanical properties of fine-grained Al2O3–ZrO2 composites consolidated by spark plasma sintering, J. Alloys Compd. 512 (2012) 63–67, https://doi.org/10.1016/J.JALLCOM.2011.09.015.

[37] E.O. Ezugwu, S.H. Tang, Surface abuse when machining cast iron (G-17) and nickel-base superalloy (Inconel 718) with ceramic tools, J. Mater. Process. Technol. 55 (1995) 63–69, https://doi.org/10.1016/0924-0136(95)01786-0.

[38] C. Xu, X. Ai, C. Huang, Fabrication and performance of an advanced ceramic tool material, Wear 249 (2001) 503–508, https://doi.org/10.1016/S0043-1648(01)00581-6.

[39] G. Upadhyaya, Materials science of cemented carbides — an overview, Mater. Des. 22 (2001) 483–489, https://doi.org/10.1016/S0261-3069(01)00007-3.

[40] R.M. Raihanuzzaman, Z. Xie, S.J. Hong, R. Ghomashchi, Powder refinement, consolidation and mechanical properties of cemented carbides — an overview, Powder Technol. 261 (2014) 1–13, https://doi.org/10.1016/J.POWTEC.2014.04.024.

[41] X. Liu, Y. Huang, J. Yang, Effect of rheological properties of the suspension on the mechanical strength of Al2O3–ZrO2 composites prepared by gelcasting, Ceram. Int. 28 (2002) 159–164, https://doi.org/10.1016/S0272-8842(01)00072-4.

[42] R.A. Cutler, A.C. Hurford, A.V. Virkar, Pressureless-sintered Al2O3-TiC composites, Mater. Sci. Eng. 105–106 (1988) 183–192, https://doi.org/10.1016/0025-5416(88)90495-8.

[43] E.O. Ezugwu, I.R. Pashby, High speed milling of nickel-based superalloys, J. Mater. Process. Technol. 33 (1992) 429–437, https://doi.org/10.1016/0924-0136(92)90277-Y.

[44] K. Zhang, J. Deng, Y. Xing, S. Li, H. Gao, Effect of microscale texture on cutting performance of WC/Co-based TiAlN coated tools under different lubrication conditions, Appl. Surf. Sci. 326 (2015) 107–118, https://doi.org/10.1016/j.apsusc.2014.11.059.

[45] A. Senthil Kumar, A. Raja Durai, T. Sornakumar, Machinability of hardened steel using alumina based ceramic cutting tools, Int. J. Refract. Metals Hard Mater. 21 (2003) 109–117, https://doi.org/10.1016/S0263-4368(03)00004-0.

[46] C.S. Kumar, S.K. Patel, Effect of duplex nanostructured TiAlSiN/TiSiN/TiAlN-TiAlN and TiAlN-TiAlSiN/TiSiN/TiAlN coatings on the hard turning performance of Al2O3-TiCN ceramic cutting tools, Wear 418–419 (2019) 226–240, https://doi.org/10.1016/J.WEAR.2018.11.013.

[47] A. Das, S.K. Patel, T.K. Hotta, B.B. Biswal, Statistical analysis of different machining characteristics of EN-24 alloy steel during dry hard turning with multilayer coated cermet inserts, Measurement 134 (2019) 123–141, https://doi.org/10.1016/J.MEASUREMENT.2018.10.065.

[48] A. Senthil Kumar, A. Raja Durai, T. Sornakumar, Wear behaviour of alumina based ceramic cutting tools on machining steels, Tribol. Int. 39 (2006) 191–197, https://doi.org/10.1016/J.TRIBOINT.2005.01.021.

[49] J.G. Corrêa, R.B. Schroeter, Á.R. Machado, Tool life and wear mechanism analysis of carbide tools used in the machining of martensitic and supermartensitic stainless steels, Tribol. Int. 105 (2017) 102–117, https://doi.org/10.1016/J.TRIBOINT.2016.09.035.